International Journal of Heat and Fluid Flow 117 (2026) 110038

Contents lists available at ScienceDirect

International Journal of Heat and Fluid Flow

journal homepage: www.elsevier.com/locate/ijhff

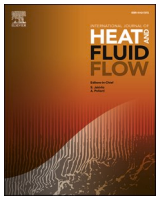

Numerical simulation of gas quenching process for molten steel slag based on VOF to DPM model

Jiahao Zhang [a,b,1], Jingcai Chang [a,b,1,*], Yuke Li [c], Zongqiang Li [d], Taiyang Liu [a], Fenghua Wei [e], Peng Wang [f], Hongfei wu [a]

[a] School of Environmental Science and Engineering, Shandong University, Qingdao 266237, Shandong, China
[b] School of Industrial Technology Research Institute, Shandong University, Weihai 264209
[c] Department of Water Management, Faculty of Civil Engineering and Geosciences, Delft University of Technology, Stevinweg 1, 2628 CN Delft, the Netherlands
[d] National Energy (Shandong) Energy Environment Co., LTD, Jinan 250000, Shandong, China
[e] Assets and Laboratory Management Office, Shandong University, Qingdao 266237, China
[f] School of Nuclear Science, Energy and Power Engineering, Shandong University, Jinan 250000, Shandong, China

ARTICLE INFO

Keywords:
VOF to DPM
Steel slag jet
Granulation and crushing

ABSTRACT

Gas quenching granulation is one of the most important modern methods utilized in molten steel slag (MSS) treatment, more positive and accurate simulated methods play a crucial role in guiding the whole gas quenching which dominate the stability, cementitious activity, magnetic separation of Magnetite and sensible heat recovery of MSS products, etc. However, the frequently used Volume of Fluid (VOF) methods can only predict the fragmentation process, but there appeared much deviation in identifying and calculating subsequent particle fragmentation and particle size distribution changes. To address these noticeable deviations, the VOF to DPM model is innovatively introduced to clarify the morphological spatial and temporal evolution for MSS by designing a transition from the continuous phase to the discrete phase for the divergent liquids. The DPM model is expert in tracking MSS particles in DPM form, and the motion, size changes, particle concentration and size distribution of divergent liquids were real-time counted and measured. Compared to the on-site particle size obtained using the air-quenching at Zhengfeng Steel Plant in China, the relative error between the two was less than 10%. The morphological spatial and temporal evolutions of MSS in the main body region, non-mutual adhesion region and particle field region were systematically studied from qualitative and quantitative aspects under different working conditions. Finally, scientific data was provided to optimize process parameters and improve granulation efficiency. These research findings provide valuable universal applicability in all the fields of gas quenching and fragmentation process and lay a theoretical foundation for subsequent strictly controlled granulated particles.

1. Introduction

Steel slag is a byproduct of industrial steelmaking, with an average production of 130–200 kg of steel slag per ton of steel (Li et al., 2024; Gao et al., 2023). According to data from the World Steel Association, China produced 1.019 billion tons of crude steel in 2023, thus producing 168 million tons of steel slag and emitting a large number of CO2 (Li et al., 2023; Lv et al., 2022; Wang et al., 2010). At present, typical slag disposal techniques include water stew, gas quenching, hot-stuffing, shallow trays, and rotary drum methods. Among them, water stew as the main simply equipped technique provides slower cooling processes, which leads to higher water consumption of 0.8–1.2 t per ton of MSS, poor stability (with *f-CaO* and *f-MgO* in the slag expanding by 96 % and 148 %, respectively, after hydration) and low cementitious activity (complete mineral phase development and coarse grains caused by slower cooling processes). This means a lower level for the coupling resource utilization of material and sensible heat of MSS, which exacerbates environmental pressures (Srivastava et al., 2023; Wu et al., 2021; Yao et al., 2023; Gu et al., 2024; Dayioglu, 2024; Zhang and Ma, 2022; Safavi Nick et al., (2021) 1144.; Yang et al., 2024). Previous studies showed that more technical rapid cooling methods such as dry gas quenching MSS were advantageous to the formation of *M1* or *M3*

* Corresponding author.
E-mail address: changjingcai@sdu.edu.cn (J. Chang).
[1] These authors contributed equally to this work and should be considered co-first authors.

https://doi.org/10.1016/j.ijheatfluidflow.2025.110038
Received 31 January 2025; Received in revised form 15 June 2025; Accepted 1 September 2025
Available online 9 September 2025

types of C_3S and to inhibit *f-CaO* and *f-MgO* generation (Zhang, 2023), and have remarkable simultaneous advantages in reducing water consumption and sensible heat recovery. The cementitious activity issues of slag products disposed of by gas quenching showed significant improvement under the premise of MSS-safe solidification (Liu et al., 2022). Therefore, gas quenching MSS has been the focus of extensive research both domestically and internationally based on the strong quenching process induced by the gas medium. For the gas quenching process, the microstructure evolution of MSS is an especially complex procedure a function of many factors, and the granulation and quenching characteristics are crucial points that would effectively dominate the cementitious activity of slag products, magnetic separation of Magnetite (MFe) and the efficiency of heat recovery, and ensure equipment security and avoid potential risks (Sakhvadze et al., 2021; Özbay and Erdemir, 2016). Owing to the complex and severe experimental conditions, coupled with the morphological, temperature and phase state spatial and temporal evolution for MSS, the well-defined particle, temperature, concentration and velocity fields were certainly difficult. Simulation calculation methods have enormous advantages in obtaining the above transient response during the whole course of the quenching process (Judd et al., 2024; Wu et al., 2023; Anderson et al., 2018); and can be used for guiding the whole gas quenching technology.

In recent simulation studies, due to the constraints of software algorithms and computational load, the granulation process of MSS using gas quenching is often modeled using a two-dimensional granulation chamber plane as the physical simulation model (Foti et al., 2020; Wang, 2021). For example, Long et al. conducted numerical simulations of the granulation process under different conditions using the CFD method, discovering that the jet impact kinetic energy and flow field distribution significantly affect the granulation characteristics (Long et al., 2013). Shi et al. conducted a numerical simulation of the two-dimensional gas quenching process of MSS using Fluent, clarified the effects of nozzle diameter, nozzle angle and jet wind speed on the distribution range of slag droplets, thereby providing data references for improving the gas quenching process (Ming, 2021). However, for the MSS fragmentation issue, two-dimensional simulations appeared insufficient to provide sufficient results. To gain a deeper understanding of the morphological evolution and fragmentation mechanisms of MSS under aerodynamic forces, while making the gas quenching simulation process more consistent with practical conditions. Wang et al. (Wang et al., 2020) established a three-dimensional rectangular granulation chamber, and they employed the Coupled Level Set and Volume of Fluid (CLSVOF) method to simulate the fragmentation of the molten slag liquid film during gas quenching. The results indicated that the MSS liquid column quickly formed a liquid film under the combined effect of K-H instability fluctuations and R-T instability fluctuations, and the thickness of the liquid film had an exponential relationship with the gas flow velocity, the mass flow rate and the viscosity of MSS. It was worth noting that the criteria for evaluating the gas quenching of MSS should not be limited to the changes in the slag surface morphology. The film size information and particle size distribution of MMS can also reflect the effectiveness of quenching characteristics. This was a more important indicator for assessing the granulation of MSS under gas quenching conditions, and in some areas, the evolvement of fragmentation is quite sensible to numerous features of the whole technology, and the so-called butterfly effect can be found for stability, cementitious activity, magnetic separation of MFe and sensible heat recovery of MSS, etc. However, the VOF model did not address this aspect; it was primarily used to capture the gas–liquid interface in multiphase flow. Although it could predict the fragmentation process of fluids and generate liquid fragments, furthermore, the parametric information of the liquid fragments obtained from this model often showed significant discrepancies with experimental data. Liu et al (Liu et al., 2022). used the VOF model to simulate the gas quenching and fragmentation process of MMS. They compared the simulated particle size distribution with the experimental results and found a significant relative error, particularly for particles larger than 5 mm, where the relative error exceeded 60 %. How to solve these noticeable deviations or erroneous, and further improve the deep understanding of the gas quenching process of MSS, becomes a critical problem in the gas quenching field.

Based on the above analysis, we dare to try to use the VOF to DPM model to gas quenching MSS for the first time, aiming to clarify the instantaneous morphological spatial and temporal evolution for MSS under aerodynamic quenching. This model has been widely applied in the fields of energy and chemical engineering to address critical issues in multiphase flow, including phase transition, cross-scale flow, and particle–fluid coupling (Liu et al., 2025; Liu and Ke, 2022; Harizi et al., 2024). Sun et al. (Sun et al., 2024) employed the VOF to DPM model to simulate droplet splashing behavior in steelmaking converters, successfully predicting the droplet splashing rate and identifying key factors influencing droplet mass ejection. Similarly, Liu et al. (Liu et al., 2023) conducted a numerical simulation of fuel flow inside a centrifugal nozzle and its external atomization process using the VOF to DPM model. Their results demonstrated that the VOF to DPM model can accurately capture both the internal flow characteristics of the centrifugal nozzle and the external atomization behavior. For this study, the detailed fragmentation and the size distribution of MSS further lay a foundation for temperature, phase state and reaction field for various gas quenching research. In addition, the new model enabled the efficient transition of MSS from a liquid continuous phase to a discrete phase, allowing dynamic tracking of MSS particles in DPM form. Through real-time counting and measurement, the deviations or errors in describing the quantity and size of the liquid blocks were significantly reduced. Compared to the on-site particle size obtained using the air-quenching at Zhengfeng Steel Plant in China, the relative error between the two was less than 10 %. In terms of computation, by utilizing adaptive mesh technology, we innovatively captured the detailed fragmentation information of MSS under high-resolution grids with lower computational load. In this paper, the morphology and structure of MSS were regionally processed and quantitatively analyzed, and the intrinsic relationship between the fragments in the main body region and the discrete liquid blocks in the non-mutual adhesion region was elucidated. Additionally, the study discussed the impact of different working conditions on these characteristics and the granulation mechanism of MSS. These research findings provide valuable universal applicability in all the fields of gas quenching and fragmentation process and lay a theoretical foundation for subsequent strictly controlled granulated particles. These more positive and accurate simulated methods would be of great significance to MSS treatment and other powder metallurgy.

2. Physical and mathematical models

2.1. Geometric model

The granulation chamber is a rectangular box with 540 mm × 300 mm × 300 mm (Fig. 1, left), modeled using ANSYS SpaceClaim software. A circular inlet with a diameter of 3 mm is constructed at the top of the chamber to serve as the inlet for the MSS. To achieve a full-phase fragmentation simulation, the left side of the chamber is defined as the gas velocity inlet, the bottom as a wall, and all other planes as pressure outlets. In selecting the dimensions of the chamber, we referred to model parameter settings from other gas-quenching slag processes. Unlike previous setups, this work increased the overall size of the granulation chamber to more accurately and extensively capture the dispersion of the slag particles.

The computational domain is meshed using structured hexahedral elements (Fig. 1, right). Six different mesh sizes are tested for independence verification (as shown in Table 1 and Fig. 2.), based on the number of particles generated under varying mesh densities. This is because, in the VOF to DPM framework, the primary “output” of the VOF stage is the breakup of the continuous-phase molten slag jet into discrete fluid chunks. In other words, the VOF model must accurately resolve the

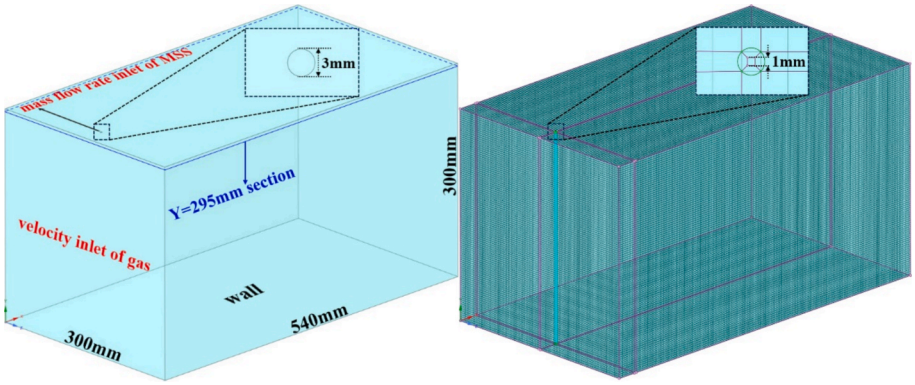

Fig. 1. Physical model of the granulation chamber (left) and initial grid division (right).

Table 1
Relationship between grid density and initial grid number and initial grid size.

Density of grid	Initial grid number (million)	Initial grid size (mm)
Coarser mesh	0.3597	6.00
Coarse mesh	0.7343	4.50
Medium mesh	1.1846	3.75
Fine mesh	1.8004	3.00
Finer mesh	2.6992	2.75
Extremely fine mesh	3.5149	2.50

liquid film and jet interface before the transition from the continuous phase to the discrete phase can occur. Because the VOF formulation is responsible for capturing jet stretching to form thin liquid films, film rupture to create ligaments, and ligament breakup to generate fluid chunks, its prediction of the continuous-phase breakup details is highly sensitive to the local mesh size. Once the continuous-phase liquid film, ligaments, and fluid chunks meet the equivalent volume and non-sphericity criteria required for the VOF to DPM transition, trackable DPM discrete particles are generated. Consequently, the total number of DPM particles produced serves as a direct measure of how finely the liquid film and ligaments have been resolved and how many fluid chunks have been formed. In brief: if the mesh is too coarse, small ligaments and fluid chunks cannot be resolved, and the number of generated discrete particles will decrease; conversely, if the mesh is overly refined, finer fragmentation details can be captured, but at the cost of a significant increase in computational time. Therefore, we selected the number of discrete particles as our grid-independence metric. We observed that once the initial mesh exceeds 1.8004×10^6 cells, further refinement changes the total number of discrete particles by less than 3.21 %. This threshold thus indicates that the VOF breakup details and the subsequent conversion to DPM particles become effectively mesh-independent. Considering the important characteristics of the MSS jet, the mass flow rate of MSS is locally refined at the inlet. Since the simulation involves the interaction between high-velocity gas flow and MSS jets, a multiphase flow model is required. Therefore, a Pressure-Based Solver (PBS) is selected. The PBS is commonly used in multiphase flow simulations involving incompressible or weakly compressible phases, particularly when phase interaction, volume fraction tracking (e.g., via the VOF and the VOF to DPM model), and surface tension effects are significant. In our case, the VOF model was adopted to capture the gas–liquid interface between the MSS and the gas phase. The PBS is well-suited for such problems because it efficiently handles the pressure–velocity coupling in flows with strong interface dynamics and is widely supported in established CFD platforms for VOF-based multiphase modeling.

2.2. Mathematical model

2.2.1. Continuous phase mathematical model

In the first stage of gas quenching steel slag, the system involves both gas and MSS phases, constituting a typical gas–liquid two-phase flow. It is essential to ensure that the sum of the volume fractions of these two phases within the control volume of the mesh satisfies the following conditions:

$$\alpha_{gas} + \alpha_{liquid} = 1 \tag{1}$$

where α_{gas} is the volume fraction of gas and α_{liquid} is the volume fraction of MSS.

Additionally, the gas–liquid two-phase system must satisfy the momentum conservation equations. By solving a single momentum equation throughout the computational domain and sharing the resulting velocity field among all phases, the momentum equation considers the

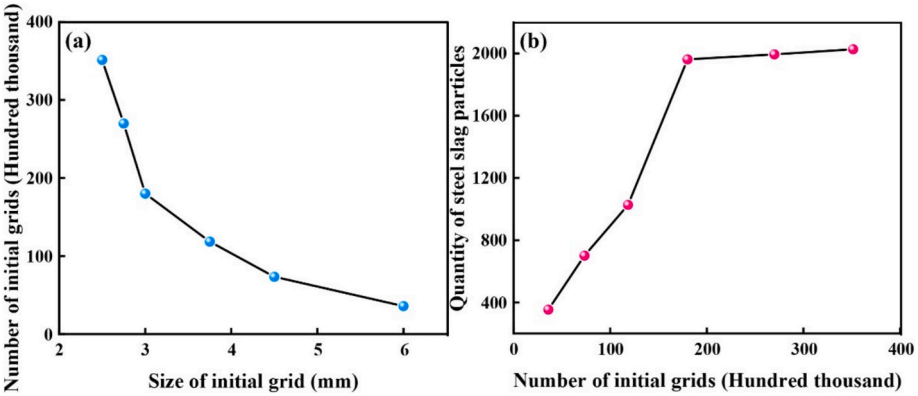

Fig. 2. Initial grid size and initial number of grids (a); initial number of grids and number of steel slag particles (b).

volume fractions of all phases with properties ρ and μ, expressed as follows:

$$\frac{\partial}{\partial t}(\rho u_i)+\frac{\partial}{\partial x_j}\left(\rho u_i u_j\right)=-\frac{\partial_p}{\partial x_i}+\frac{\partial \tau_{ij}}{\partial x_j}+\rho g_i+F_i \tag{2}$$

where p is the hydrostatic pressure (Pa), ρ is the density of the fluid (kg/m^3), u_i and u_j are the velocity components (m/s), τ_{ij} is the stress tensor (N/m^2), g_i is the gravitational volumetric force (N), and F_i is the external volumetric force (N).

High-velocity gas granulation of MSS is an extremely complex turbulent flow process. The SST k-ω model is chosen to simulate the high-speed flow process. The control equations of turbulent kinetic energy k and turbulent dissipation rate ω are as follows:

$$\frac{\partial}{\partial t}(\rho k)+\frac{\partial}{\partial x_i}(\rho u_i k)=\frac{\partial}{\partial x_i}\left[(\mu+\sigma_k\mu_t)\frac{\partial k}{\partial x_i}\right]+P_k-\rho\varepsilon \tag{3}$$

$$\frac{\partial}{\partial t}(\rho \omega)+\frac{\partial}{\partial x_i}(\rho u_i \omega)=\frac{\partial}{\partial x_i}\left[(\mu+\sigma_\omega\mu_t)\frac{\partial k}{\partial x_i}\right]+P_\omega-C_{lim}\rho\omega^2 \tag{4}$$

where k is the turbulent kinetic energy (m^2/s^2), μ_t is the turbulent dynamic viscosity (Pa·s), σ_k and σ_ω are correction factors, P_k is the turbulent energy production term, P_ω is the turbulent dissipation rate production term, $\rho\varepsilon$ is the turbulent dissipation rate (m^2/s^3), C_{lim} is the limiting factor, which is used to limit the growth of the turbulent dissipation rate usually taking values between 0.4 and 0.8. The SST k-ω model constants are set as $\sigma_{k,1}=1.176$, $\sigma_{\omega,1}=2.0$, $\sigma_{k,2}=1.0$, $\sigma_{\omega,1}=1.168$, $\alpha_1=0.31$, $\beta_{i,1}=0.075$, and $\beta_{i,2}=0.0828$.

2.2.2. Discrete phase mathematical model

In the second stage, the continuous MSS phase transitions into a discrete particle phase. These transformed steel slag particles are also subject to the balance of forces and the energy equation. The force balance equation for the steel slag particles in a Cartesian coordinate system is as follows:

$$m_p\frac{d\vec{u_p}}{dt}=m_p\frac{\vec{\nu_l}-\vec{u_p}}{\tau_r}+m_p\frac{\vec{g}\left(\rho_p-\rho\right)}{\rho_p}+\vec{F} \tag{5}$$

where m_p is the particle mass (kg), $\vec{u_p}$ is the particle velocity (m/s), $\vec{\nu_l}$ is the velocity of MSS (m/s), $\frac{\vec{\nu_l}-\vec{u_p}}{\tau_r}$ is the drag force (N), ρ_p is the density of particle (kg/m^3), τ_r is the relaxation time (s) calculated by:

$$\tau_r=\frac{4\rho_p d_p^2}{3\mu C_d R_e} \tag{6}$$

where d_p is the particle diameter (m), C_d represents the drag coefficient between the gas and the particle. Since the particles produced are smooth spheres, a spherical drag model is used:

$$C_d=a_1+\frac{a_2}{R_e}+\frac{a_3}{R_e^2} \tag{7}$$

where a1, a2, a3 use different constants for different Re numbers according to Moris and Alexander, and R_e is the relative Reynolds number (Morsi and Alexander, 1972), which is defined as:

$$R_e=\frac{\rho d_p\left|\vec{u}_p-\vec{\nu_l}\right|}{\mu} \tag{8}$$

2.3. The validation of simulation

VOF to DPM model was first used as modeling technology to simulate the gas quenching for the first time in a gas quenching molten state material area. In this study, both the VOF to DPM model and the VOF model were employed to simulate the gas quenching process of molten slag. The fragmentation behavior of the slag was compared under identical conditions: gas quenching velocity of 200 m/s, slag viscosity of 0.25 Pa·s, mass flow rate of 0.1 kg/s, and density of 3200 kg/m^3. The objects measured by the two different models are indicated by asterisks in Fig. 3. In addition, to verify the authenticity of the simulation, this study conducted on-site sampling of gas-quenching steel slag from the Zhengfeng steel plant. The particle size distribution of the gas quenching MSS was obtained through screening, and this information was compared with the particle sizes obtained from the simulation. As shown in Table 2, the proportion of particles in the steel slag at the Zhengfeng steel plant with a size greater than 0.88 mm is 33.76 %, while the proportion of particles with a size between 0.25 mm and 0.88 mm is 61.75 %. In gas quenching for this simulation, the proportion of particles smaller than 0.25 mm was almost zero, the proportion of steel slag larger than 0.88 mm was 23.19 %, and the size of most particles ranged from 0.25 mm to 0.88 mm. The primary reason for this discrepancy was that, during the simulation, the viscosity and surface tension of the MSS were assumed to be constant values. In actual industrial processes, however, the physical properties of the slag continuously vary with temperature specifically, the viscosity increases as the slag cools down, making it less prone to further fragmentation. Moreover, when converted into the DPM particle phase, the DPM model by default neglects effects such as particle collision, coalescence, and secondary fragmentation. In reality, during the gas quenching process, slag particles may undergo secondary agglomeration or breakage due to changes in viscosity or disturbances from the gas flow. It is worth noting that the slag particle size distribution generated by modifying the mesh density showed only slight variations. Therefore, mesh density is not considered the primary factor contributing to the discrepancies between the simulation and experimental data. However, compared with the particle size distribution of steel slag obtained by the VOF model, the particle size obtained by the VOF to DPM model was more in line with the actual situation and closer to the particle size distribution of gas quenching steel slag obtained by industrial production.

3. Numerical methods

3.1. Calculating the mechanism of VOF to DPM model

The simulation of the MSS gas quenching process in this study was conducted using Ansys Fluent (version 2024R1). The VOF model was used to simulate the gas quenching process of MSS, as shown in Fig. 4. From the figure, it can be observed that in Region A (main body region), the MSS jet was impacted by high-speed airflow. Due to the influence of the airflow, the slag jet was stretched and thinned, forming a liquid film. This process involves the interaction between the airflow and the slag jet, where the impact, friction and shear forces of the airflow cause disturbances on the jet surface, gradually expanding it into a film structure. In Region B (torn liquid film region), the process of the liquid film tearing to form liquid ligaments was illustrated. When the liquid film continues to be subjected to airflow, it starts to exhibit unstable oscillations due to the combined effects of surface tension and aerodynamic forces, eventually tearing and forming liquid ligaments. In Region C (liquid ligaments region), the disturbance of the liquid ligaments by the airflow was further intensified. The central parts gradually contract to form troughs, decrease the structural stability and ultimately eventuate the ligaments' disintegrating into discrete liquid blocks. By measuring the dimensions of the discrete liquid blocks, it was found that the average size of the discrete liquid blocks is 2.6 mm. However, the VOF model can only predict the fragmentation process of MSS. It cannot calculate the subsequent particle fragmentation and particle size distribution changes. Therefore, the discrete liquid blocks obtained cannot be fully used as indicators to evaluate the effectiveness of gas quenching.

The VOF to DPM model effectively combines the advantages of the VOF and DPM model. The VOF model uses explicit discretization methods, such as geometric reconstruction, to track the gas–liquid interface, providing better predictions of liquid fragmentation

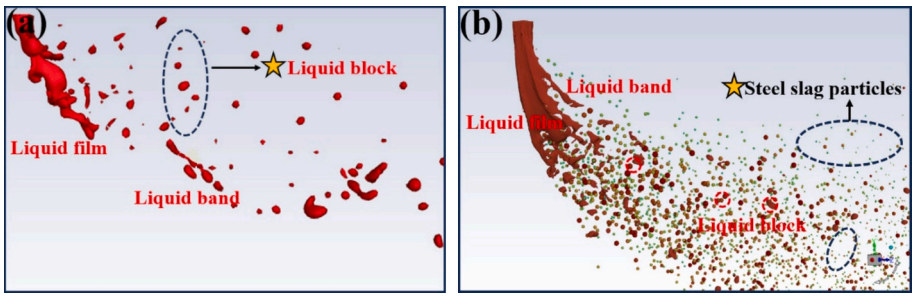

Fig. 3. Schematic representation of the target (indicated by a star) selected for particle size analysis using the VOF model (a) and the VOF to DPM model (b).

Table 2
Comparison of steel slag particle size distribution.

	>0.88 mm	0.25 ~ 0.88 mm	<0.25 mm	Average diameter	Viscosity
Zhengfeng steel slag	33.76 %	61.75 %	4.49 %	0.653 mm	0.1 ~ 0.5 Pa·s
VOF to DPM model(1.8004 million)	23.19 %	76.74 %	0.07 %	0.583 mm	0.25 Pa·s
VOF to DPM model(2.6992 million)	22.87 %	77.04 %	0.09 %	0.581 mm	0.25 Pa·s
VOF model	58.77 %	41.17 %	0.06 %	1.345 mm	0.25 Pa·s

processes. The DPM model, on the other hand, can accurately capture particle-related information with lower computational costs. Regarding the issue of simulated costs and accuracy, using the VOF model to simulate the slag granulation process, takes 140 h to calculate 0.5 ms, while using the VOF to DPM model simulation takes about 24 h. When calculating the same time interval, the VOF to DPM model reduces computation time by 483.33 % compared to the VOF model. As the computation time increases, the time difference between the two models becomes increasingly significant. This is because, as time progresses, more fragmented details are revealed (e.g., the capture and tracking of small liquid droplets in the continuous phase), and these fragmented details require an adaptive mesh to provide a more refined grid. In contrast, the VOF to DPM model can convert these small liquid droplets into discrete phase particles. After conversion, the fine mesh automatically adjusts and returns to the initial mesh size, significantly reducing the overall computational workload and computational time of the example. In addition, the Mean Particle Diameter Deviation (MPDD) was used to compare the particle diameters obtained from the two different models with the experimentally obtained particle diameters. The results showed that the MPDD of the VOF to DPM model was 12.01 %, while that of the VOF model was 51.45 %. It can be seen that modifying the VOF model to the VOF to DPM model, not only saves time but also significantly improves the prediction accuracy of the granulation process. The transformation mechanism and schematic of the VOF to DPM model are shown in Fig. 5. Before the simulations, we calibrated the parameters of the VOF to the DPM model. This mainly included the

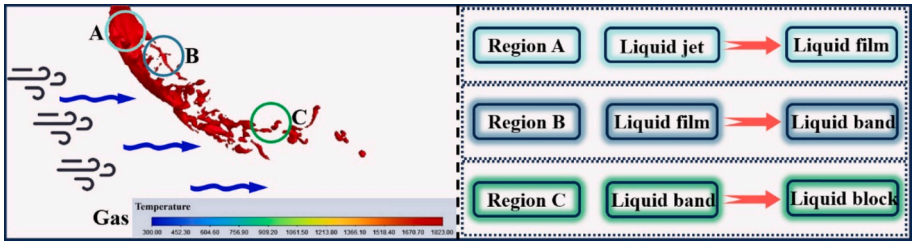

Fig. 4. Gas quenching process of MSS under VOF model.

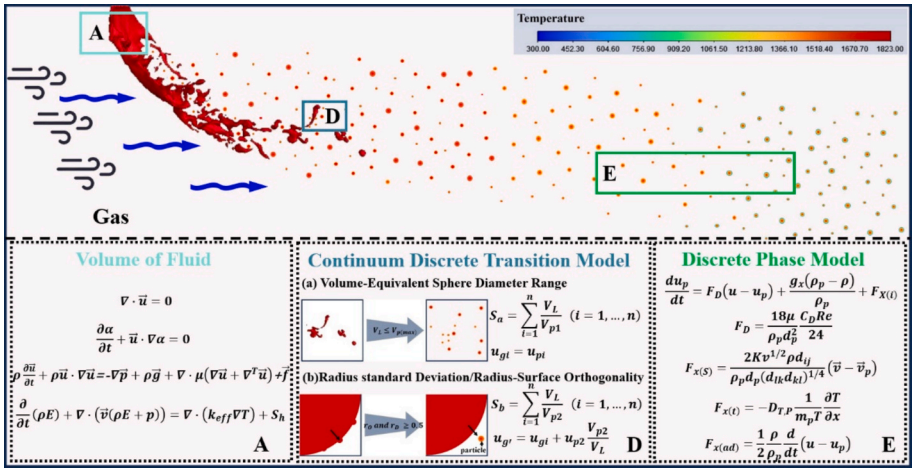

Fig. 5. Calculating mechanism of VOF to DPM model in the gas quenching process.

adjustment of the fluid interfacial tension and the review of the motion characteristics of the generated particles in the chamber. The rationality of the fluid-particle interaction was ensured. In the VOF and VOF to DPM model, the volume fraction equation is discretized using an explicit scheme, which is widely adopted due to its capability to track the sharp interface between phases with high temporal resolution (Garoosi and Hooman, 2022; Hirt and Nichols, 1981). This facilitates accurate capture of the transient behavior and interface evolution in multiphase flow simulations. The volume fraction truncation parameter is set to1×10^{-6}, and the Courant number is 0.25. In Region A (main body region), the VOF model was used to simulate and predict the initial jet tearing to form liquid ligaments and the subsequent breakup of these ligaments into droplets. In the early stages, particle clusters representing droplets move together as a continuous liquid phase. As particle clusters and the continuous liquid phase pass through certain regions, their paths may gradually diverge. In Region D (non-mutual adhesion region), the VOF to DPM model automatically detected the divergent liquid that has separated from the core region and evaluated its conversion. If the liquid fragments met the criteria of equivalent volume and non-sphericity, the corresponding liquid mass was removed from the VOF model and converted into particles within the Lagrange framework. In Region E (particle field region), where the transition from the continuous phase to the discrete phase was completed, the DPM model was used to track the motion and size changes of the steel slag particles, and particle concentration and size distribution were measured and analyzed in fully developed particle field. However, it should be noted that this model also has certain limitations. For instance, after the transition to the DPM phase, the microscale interfacial dynamics captured by the original VOF model, such as the oscillations of the liquid film or the expansion of micropores, may be simplified into statistical characteristics of discrete particles. As a result, some detailed mechanisms of fragmentation may not be fully preserved (Li et al., 2023). At the same time, the simplification of complex physical phenomena may affect the accuracy of the simulation results. For example, the trend of increasing particle size in high-viscosity slag could be underestimated due to the simplified assumptions in the DPM model (Di Martino et al., 2022).

Finally, regarding the algorithm selection for the VOF to DPM model calculations, the PISO algorithm was adopted. This algorithm employs multiple pressure correction steps, which significantly reduce pressure residuals and help prevent numerical divergence caused by interface deformation or interphase interactions. Moreover, it allows for stable simulations even with relatively large time steps, particularly when using adaptive time stepping, thus achieving a balance between computational accuracy and efficiency (Yan et al., 2025).

3.2. The utilization of adaptive mesh refinement technology

In this paper, the VOF to DPM model was used in conjunction with adaptive mesh refinement (AMR) technology. AMR automatically adjusted the size and number of computational grids in response to real-time changes in the solution to enhance numerical efficiency and accuracy (Pappa et al., 2024; Chen et al., 2024; Xu et al., 295 (2024)). The implementation process of AMR is illustrated in Fig. 6. Irigaray et al (Irigaray et al., 2024). employed CFD to analyze vehicle aerodynamics and successfully optimized the mesh in targeted regions using AMR, significantly reducing computational resource requirements. Similarly, Yan et al (Yan et al., 2025). demonstrated that the integration of the VOF method with adaptive mesh refinement can accurately capture the gas–liquid interface while minimizing the total number of mesh cells. Currently, there are three refinement criteria for AMR: gradient-based, value-based, and thickness-based methods (Foti et al., 2020). The gradient-based method can be further divided into volume fraction gradient (Sun et al., 2024; Chen et al., 2019) and density gradient methods (Heinrich and Schwarze, 2020), depending on the variables involved. In the slag fragmentation process during gas quenching, the volume fraction gradient method is more applicable primarily because the process involves intense dynamic interactions between gas–liquid phases, and the morphology of the phase interface (such as between MSS and the gas) changes rapidly and irregularly. The volume fraction gradient method captures the abrupt variation in volume fraction at the interface directly, enabling dynamic refinement of the mesh in the interfacial region (Radford, 1995; Chen and Zhang, 2016). This allows for accurate tracking of interface evolution, such as MSS breakup and droplet formation. In contrast, the density gradient method is limited by the relatively smooth variation in density within multiphase flows, which may be further affected by coupled factors such as temperature and pressure, making it less responsive in identifying interface positions (Mohan and Tomar, 2021). Threshold-based methods rely on fixed criteria, which lack adaptability to dynamically evolving interfaces, while thickness-based methods are more suited to structured regions such as boundary layers and are not well suited for irregular, dynamic interfaces. Therefore, the volume fraction gradient method offers superior accuracy and efficiency in multiphase interface tracking. AMR had been successfully applied by predefining mesh refinement and coarsening criteria, and comparing the volume fraction of the liquid phase within each cell. In this paper, the adaptive mesh encryption level is set to 6, which enables the mesh to be dynamically adapted to maximize and achieve the detailed information of slag fragmentation. The initial state and the adaptive mesh after 20 ms are shown in Fig. 7.

4. Results and analysis

4.1. Morphological spatial and temporal evolutions of MSS

Gas quenching of MSS was a complex process caused by fluid dynamics. It requires continuous optimization and adjustment of process parameters based on the product requirements. This study analyzed four factors affecting the gas quenching process of MSS, with the parameters for each case detailed in Table 3. The basis for the viscosity and density of MSS can be referred to by Long (Long et al., 2013) and Liu (Liu et al., 2022); Gu (Gu, 2021). Meanwhile, the following analysis of MSS fragmentation details was conducted using an isosurface method based on volume fraction (with a threshold set to 0.5). This method provides an intuitive visualization of the dynamic evolution of the multiphase flow interface, allowing for a clear representation of the phase boundary distribution between the molten slag and the gas. Consequently, it enables precise identification of the initial fragmentation location, fracture morphology, and the dispersion trajectory of liquid slag fragments.

Fig. 8 shows the volume fraction contour of MSS at 20 ms under different conditions. The figure illustrates the difference in morphological structure and the spread extent of the main jet caused by the influencing mechanism corresponding to these factors. Viscosity is a

Fig. 6. Schematic illustration of the mesh refinement and coarsening process of the AMR technique.

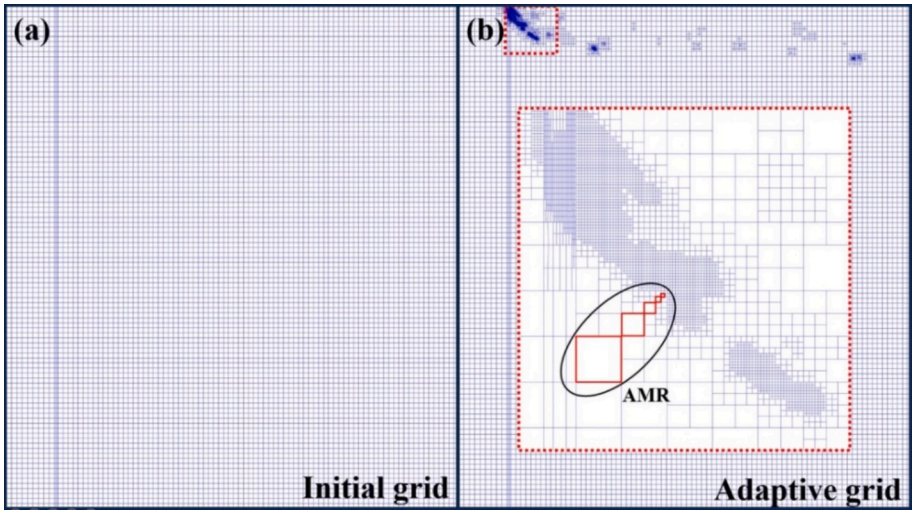

Fig. 7. Initial mesh (a) and after 20 ms of computation (b) for z = 150 mm cross-section using AMR.

Table 3
Modeling scheme under different factors in the gas quenching process.

Cases	Gas Velocity (m/s)	MSS Viscosity (Pa·s)	MSS Mass flow rate (kg/s)	MSS Density (kg/m^3)
1	50	0.25	0.10	3200
2	100	0.25	0.10	3200
3	200	0.25	0.10	3200
4	340	0.25	0.10	3200
5	200	0.50	0.10	3200
6	200	0.75	0.10	3200
7	200	1.00	0.10	3200
8	200	0.25	0.05	3200
9	200	0.25	0.15	3200
10	200	0.25	0.20	3200
11	200	0.25	0.10	2800
12	200	0.25	0.10	3000
13	200	0.25	0.10	3550

crucial indicator of MSS fluidity. Higher viscosity indicates stronger intermolecular forces and poorer fluidity, leading to difficulties in fragmenting and forming particles. As viscosity increased, the continuity of MSS improved, and fewer discrete liquid blocks detached from the main jet. This behavior was consistent with the findings from Gao (Gao et al., 2015). Regarding wind speed, slag exhibited more flattened characteristics at higher wind speeds, while at lower wind speeds, the structure tended to be more vertical. For instance, the length of the slag jet at 50 m/s was 5.82 times that at 340 m/s. This difference arises because the shear and impact forces exerted by the gas flow vary. Higher wind speeds significantly enhanced slag-liquid separation, facilitating the granulation. Mass flow rate also played a critical role in granulation effectiveness. A higher mass flow rate can lead to greater difficulty in fragmentation, while a lower mass flow rate can increase production costs. At a mass flow rate of 0.05 kg/s and wind speed of 200 m/s, the slag stream rapidly fragmented into discrete liquid blocks and distributed throughout the granulation chamber. As the mass flow rate increased, this fragmentation effect decreased, and the slag layer became more stable. At 0.20 kg/s, the length of the main slag jet significantly elongated, and the number of droplets formed by gas quenching increased. Nevertheless, it should be noted that as the mass flow rate continued to increase, fragmentation of the MSS became more difficult. As shown in Fig. 9, when the mass flow rate was 1.00 kg/s, the slag jet was significantly elongated. Although a small number of slag droplets were formed under the influence of aerodynamic force, the morphological structure of the main jet region remained intact. When the mass flow rate increased to 2.00 kg/s, the MSS jet flow exhibited almost no fragmentation, generating only a few slag droplets. The effect of aerodynamic force was completely outweighed by the inertial force of MSS, preventing further fragmentation. This greatly increased the difficulty of fragmentation and slowed the gas quenching process, leading to more prominent cooling safety issues and a higher risk of equipment damage. Steel slag density was influenced by factors such as temperature, crystalline structure, and composition, resulting in dynamic effects during gas quenching. As shown in the figure, at 0.10 kg/s, the effect of density was minimal, particularly for liquid slag with densities below 3200 kg/m^3, which exhibited similar extensibility. However, when the slag density increased to 3550 kg/m^3, both the length of the jet and the number of discrete droplets increased. This change was likely due to the reduction in volume caused by higher density, while mass remain constant.

Fig. 10 shows the spatial and temporal evolution of the morphological structure, using the volume fraction contour of MSS for analysis in Case 2. The figure demonstrated that, over time, the macroscopic morphological structure seems stabilized. From the view of microstructure, minor oscillations keep happening at the middle and lower ends of the jet, liquid film tearing and ligament break-up phenomena occur due to the combined effects of internal and external forces. These observations are consistent with Liu (Liu et al., 2022). The whole system is in a relatively stable stage of development, thus means, the continuous process of MSS fragmentation and granulation can proceed as expected.

4.2. *Quantitative analysis of the morphology and structure for MSS*

To clarify the impact of different conditions on the fragmentation effect of MSS jet. This study conducted a regional analysis of the characteristic dimensions of gas-quenching MSS at 20 ms. Additionally, a plane at Y = 295 mm was extracted to explicitly analyze the morphological characteristics of the MSS liquid film, laying the foundation for the subsequent calculation of the average liquid film thickness and the analysis of the MSS fragmentation process. As shown in Fig. 11 (a), the MSS jet was divided into two regions: the main body and the non-mutual adhesion region. The relevant characteristic dimensions of these two regions were quantified. The structural characteristics of the main body were measured using width and length, while the number of discrete liquid blocks was used to describe the non-mutual adhesion region. Fig. 11(b) illustrates the morphology of the MSS liquid film and the positional(1, 2, 3, 4, 5) used to calculate the average liquid film thickness. The length and width of the main region of the MSS jet, as well as the average film thickness at the Y = 295 mm section, were each measured three times using Image J (an image processing software), and

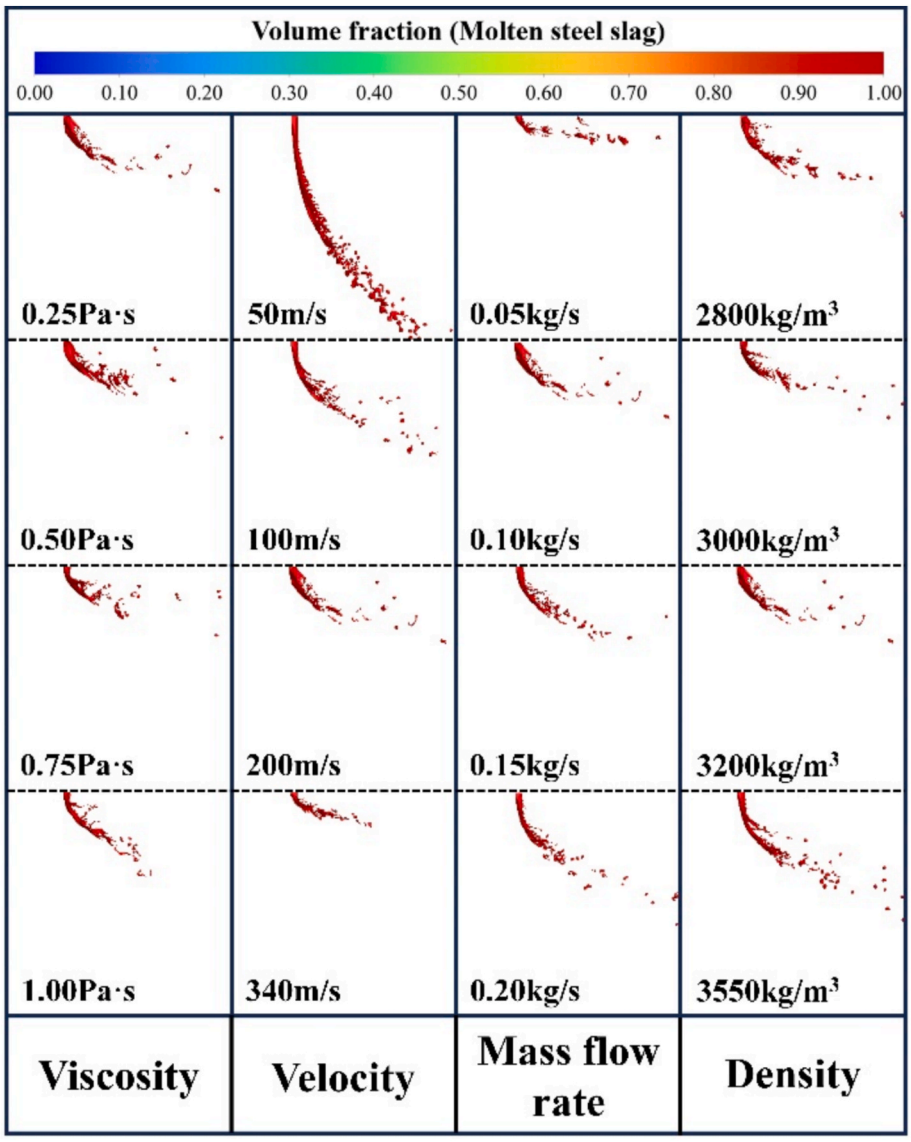

Fig. 8. Morphological characteristics of MSS under different conditions (20 ms).

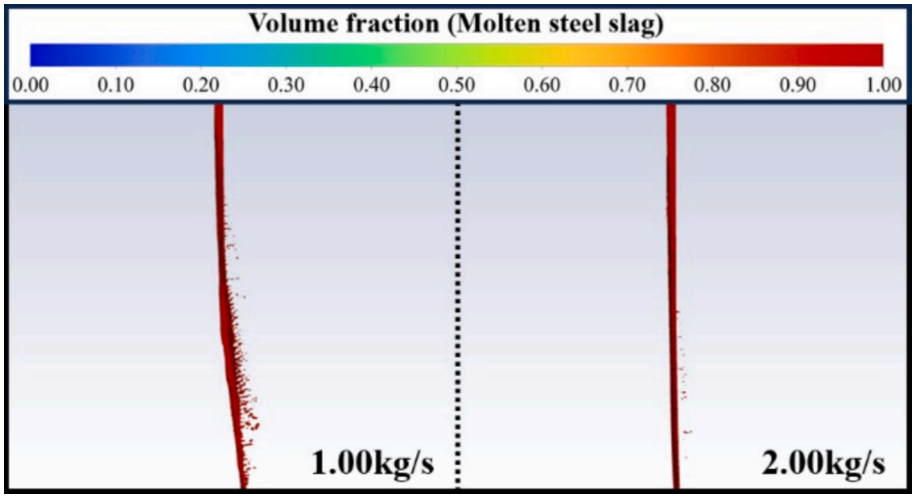

Fig. 9. Morphological characteristics of MSS under the conditions of mass flow rates of 1.00 kg/s and 2.00 kg/s.

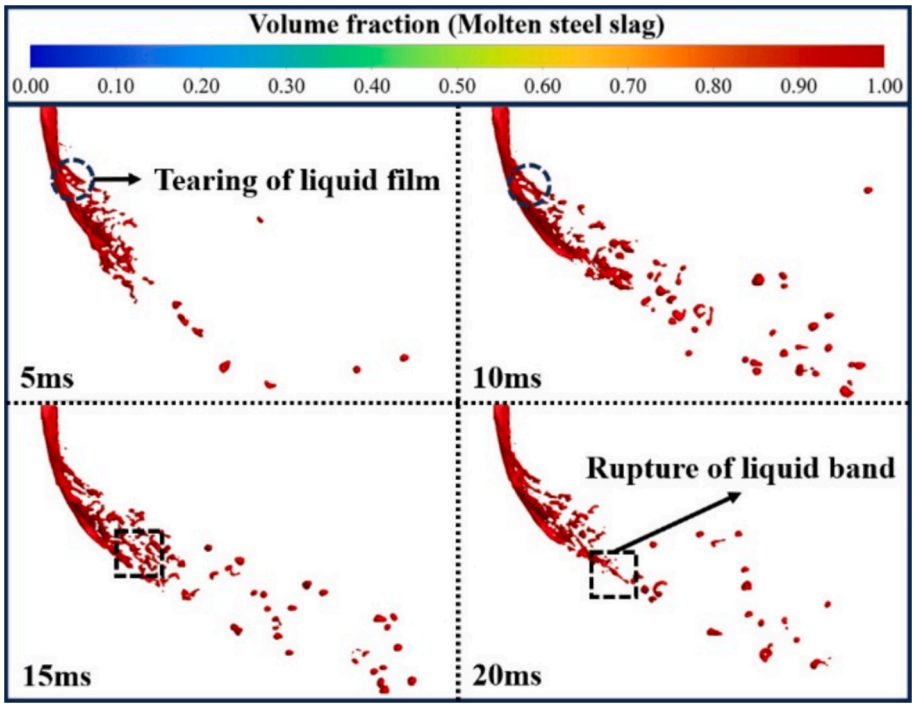

Fig. 10. Morphological spatial and temporal evolutions of MSS over time (case 2).

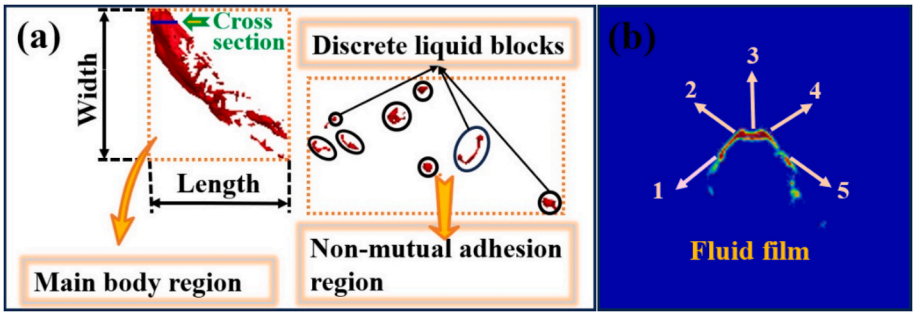

Fig. 11. Defining characteristic dimension of MSS jets (a), the morphology of the liquid film at the Y = 295 mm section (b).

the results were averaged. Through the following comprehensive analysis, detailed data feedback can be provided for the gas quenching process of MSS, which was conducive to continuous improvement and optimization of the gas quenching technology.

4.2.1. Morphology characteristics of MSS flow in main body region A

Fig. 12 (a) illustrates the significant impact of quenching wind speed on the length and width of the main body region for MSS flow. As wind speed increased, the width of the jet gradually decreased, while the length first shortened and then lengthened. At 50 m/s, the length and width reached their maximum, measuring 53.24 mm and 22.52 mm, respectively. This phenomenon was attributed to the insufficient aerodynamic force at lower wind speeds, which fails to promptly break up the MSS, causing it to stick together and elongate over time. Conversely, the increase in the length at 340 m/s was also due to the excessive effect of higher aerodynamic force. The influence of viscosity on the fragmentation effect of the main body region was more complex. Regarding the width, except for a viscosity of 1 Pa·s, the differences in the width compared to other viscosities did not exceed 15.76 %. For length, viscosities of 0.5 Pa·s and 1 Pa·s had a noticeable impact, elongating the main body region of the jet. It was worth noting that the length and the width of the MSS jet did not change regularly with increasing viscosity. This irregularity was due to the complexity of data processing, causing the main body region of 0.75 Pa·s to fracture prematurely, thus affecting subsequent data measurement. The increase in mass flow rate significantly affected the width of the main body region. The width at a mass flow rate of 0.2 kg/s was 3.35 times that at a mass flow rate of 0.05 kg/s. However, changing the mass flow rate did not cause significant fluctuations in the length. The length and the width of the jet initially decrease and then increase with increasing slag density, with width consistently exceeding length. At a slag density of 3000 kg/m^3, both the length and width reached their minimum values, measuring 10.24 mm and 11.52 mm, respectively. When the density reached 3550 kg/m^3, the difference between the length and width of the main body region was at its maximum, with the width exceeding the length by 30.75 %.

Fig. 12(b) revealed the trend and effects of different conditions on the average liquid film thickness of the MSS. As the gas quenching velocity increased, the average liquid film thickness gradually decreased, with the most significant reduction occurring when the gas quenching velocity increased from 100 m/s to 200 m/s. The viscosity, mass flow rate, and density of the MSS showed a consistent influence on the trend of the average liquid film thickness. Specifically, the average liquid film thickness increased with the rise in MSS viscosity, mass flow rate, and density. Among these factors, the viscosity of the MSS had the most significant effect on the average liquid film thickness. When the viscosity increased from 0.25 Pa·s to 1.00 Pa·s, the average liquid film thickness of

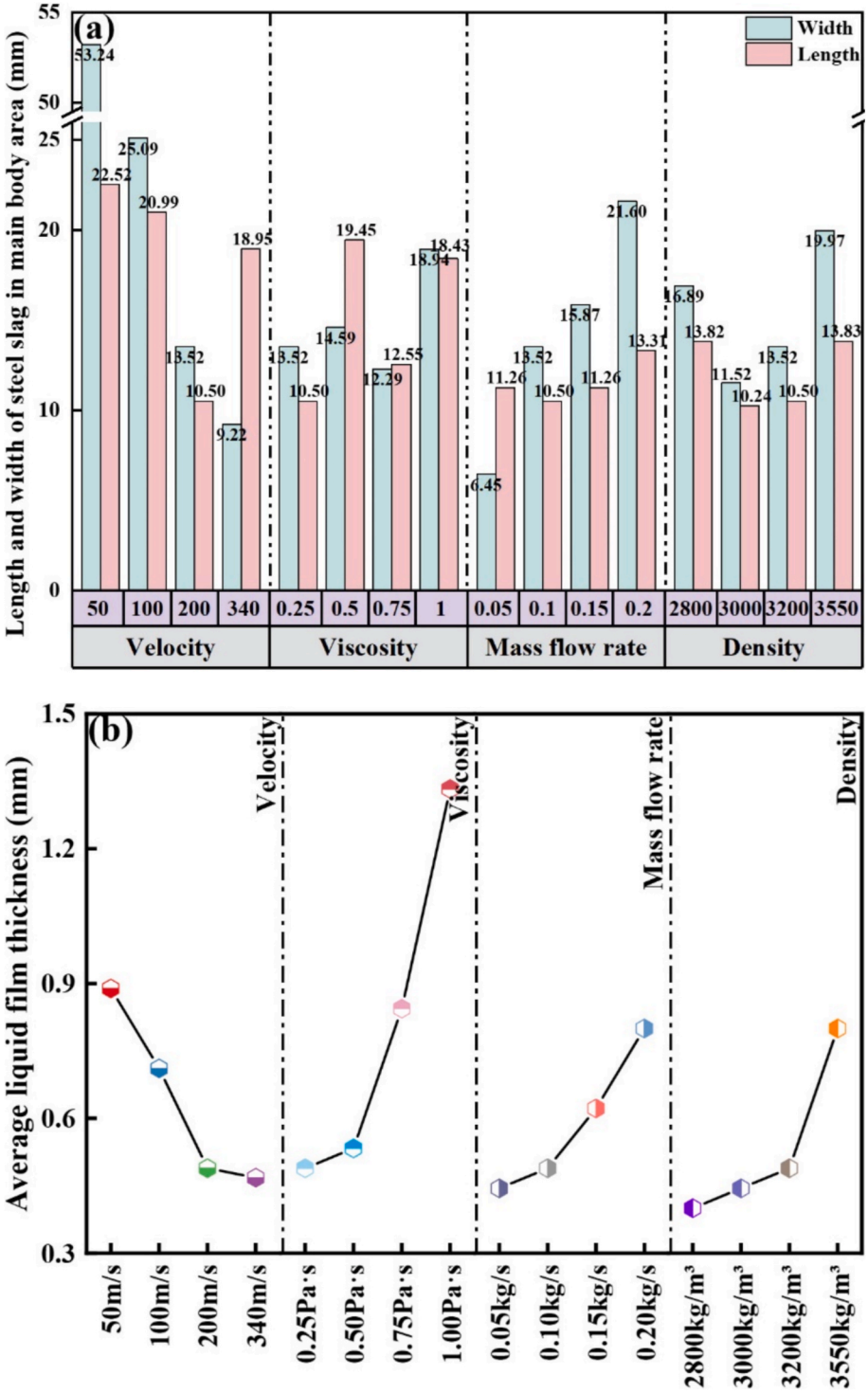

Fig. 12. Comparisons of length and width of main body region (a) and average liquid film thickness (b) for MSS under different conditions at 20 ms.

the MSS increased by 2.73 times. This indicates that a higher viscosity of MSS is more detrimental to the stretching deformation and fragmentation of the liquid film during the gas quenching process.

4.2.2. Main characteristics of discrete blocks in non-mutual adhesion region d

The number of discrete liquid blocks in the non-mutual adhesion region reflected the fragmentation effectiveness of the MSS and could significantly influence subsequent secondary granulation. It can be inferred larger size discrete liquid blocks could lead to recalescence phenomena due to latent heat, which, in severe cases, caused the fragments to adhere to the granulation chamber walls, thus reducing equipment lifespan. As shown in Fig. 13 (a), the number of discrete liquid blocks in the non-mutual adhesion region decreased with increasing gas quenching wind speed. Higher wind speeds facilitated the direct conversion of MSS into DPM-form steel slag particles. Viscosity had a less pronounced effect on the number of discrete liquid blocks, with an average of 20.5 and a standard deviation of 1.118 across the four different viscosities, indicating well data concentration. Additionally, there was a positive correlation between mass flow rate and the number

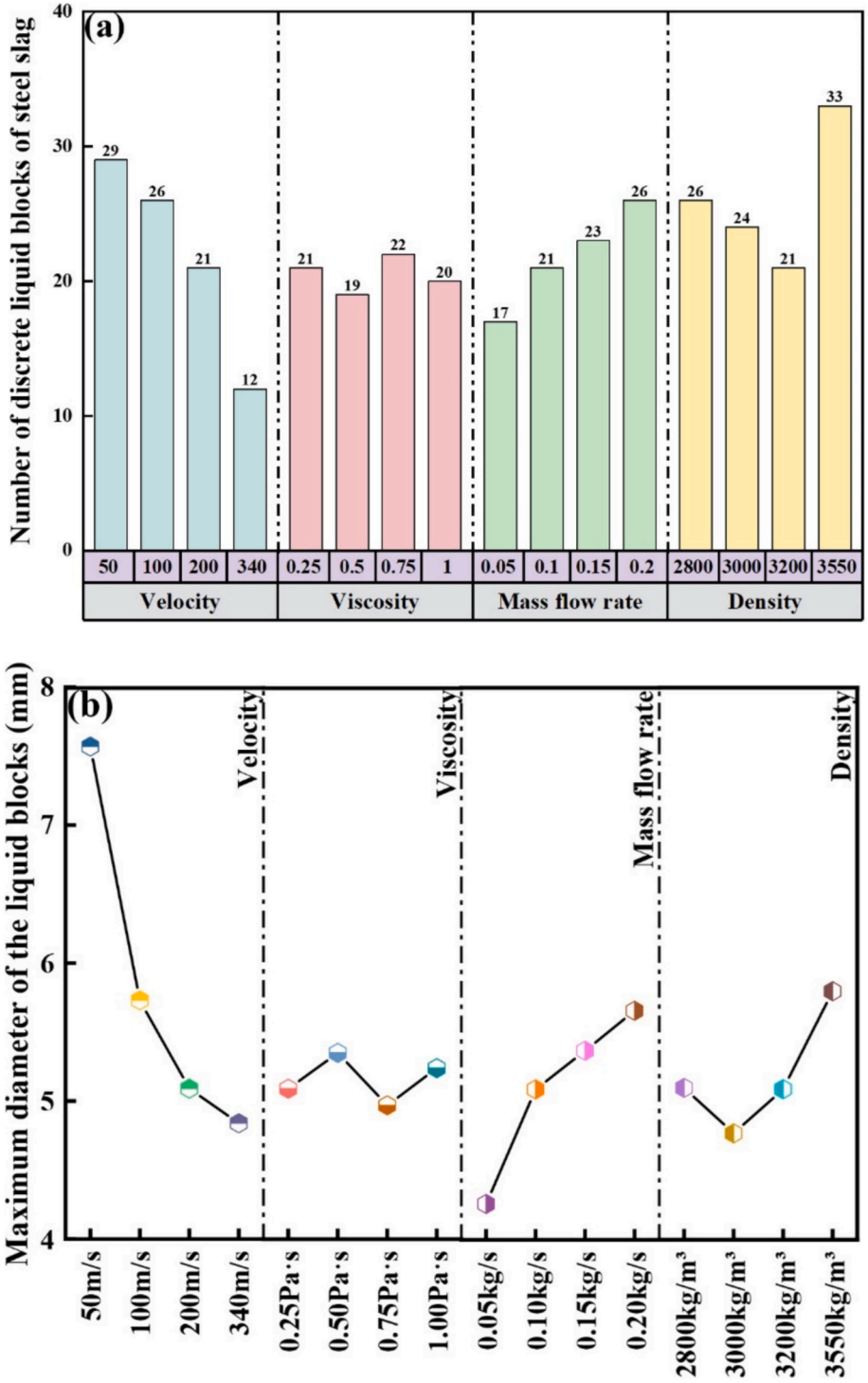

Fig. 13. Comparisons of the number (a) and maximum size (b) of discrete liquid blocks in the non-mutual adhesion region for MSS under different conditions at 20 ms.

of discrete liquid blocks; the number of blocks steadily increased with higher mass flow rates, corresponding to the increased slag flow per unit time. As the density of the steel slag increased, the number of discrete liquid blocks gradually decreased. However, when the density reached 3550 kg/m^3, the number of blocks surges, increased by 1.57 times compared to slag with a density of 3200 kg/m^3. This surge was likely due to complex interactions between inertia and fluid dynamics at higher densities. Comparing this to Fig. 12 (a), we observe that the trend of the number of discrete liquid blocks in the non-mutual adhesion region was broadly consistent with the width of the main body region of the steel slag jet. This similarity suggested that both variables were driven by similar factors, likely stemming from the fragmentation mechanism and the gas quenching process, causing synchronous temporal changes in both variables.

As shown in Fig. 13 (b), with the increase in gas quenching velocity, the maximum size of the discrete liquid blocks rapidly decreased, which is consistent with the strong fragmentation effect induced by aerodynamic enhancement. When the gas quenching velocity reached 50 m/

s, the maximum size of the discrete liquid blocks in the non-mutual adhesion region was 7.57 mm. As the viscosity of the MSS increased, the maximum size of the discrete liquid blocks exhibited fluctuating behavior. Notably, the fluctuation trend of the maximum size of the discrete liquid blocks was the opposite of the effect of viscosity on the number of discrete liquid blocks shown in Fig. 13 (a). In other words, as the number of discrete liquid blocks increased, their maximum size decreased. This might be related to the incomplete fragmentation of the liquid blocks, which could lead to an overestimation of the size statistics. The effect of mass flow rate on the maximum size of the discrete liquid blocks followed the same trend as shown in Fig. 13 (a). As the mass flow rate increased, the maximum size of the discrete liquid blocks continuously increased. When the density increased from 2800 kg/m^3 to 3000 kg/m^3, 3200 kg/m^3, and finally 3550 kg/m^3, the maximum size of the discrete liquid blocks initially decreased and then increased. The minimum maximum size of the discrete liquid blocks, 4.77 mm, was observed when the MSS density was 3000 kg/m^3. The maximum size of the discrete liquid blocks had a significant impact on the entire gas quenching process. In terms of fragmentation, larger liquid blocks made it more difficult for the slag to break down further. In terms of cooling, larger liquid blocks had a smaller surface area, resulting in slower cooling rates and poor gas quenching effects, which could lead to uneven crystallization and affect the physical properties of the steel slag.

4.2.3. Characteristics of granulated particles in particle field region e

(1) Particle size distribution of DPM particles under different conditions.

Particle size was a widely focused issue not only in the gas quenching MSS but also in the power metallurgy process. Different applications require specific particle sizes with special applications. At 20 ms during the gas quenching process, the DPM particle size data generated in Fluent were imported into Origin (2021) for analysis. As shown in Fig. 14, the particle size distribution curves of MSS under four different conditions were fitted, and the corresponding slag particle sizes at D10, D50, and D90 were obtained. Taking Fig. 14 as an example, the above operations were carried out for each case in Table 3, and the steel slag particle sizes corresponding to D10, D50 and D90 under different working conditions were obtained as shown in Fig. 15. From Fig. 15 (a), it was evident that the particle size corresponding to different cumulative distributions was negatively correlated with the gas-quenching wind speed. As the gas-quenching wind speed increased, the overall size of the slag particles decreased significantly. For example, the D10 of steel slag at a quenching wind speed of 340 m/s was 23.72 % smaller compared to that of 50 m/s, indicating that a reasonable increase in quenching wind speed could yield finer granulated particles. Contrarily, viscosity (Fig. 15 (b)) had the opposite effect on steel slag particle size compared to wind speed. Higher viscosity resulted in larger particles after quenching. This was because high-viscosity MSS has strong intermolecular forces, making it more resistant to shear fragmentation and thus making it difficult to break into fine particles. Fig. 15 (c) shows the impact of mass flow rate on steel slag particle size. The particle size corresponding to 50 % and 90 % cumulative distribution initially increased and then decreased with mass flow rate. At a mass flow rate of 0.15 kg/s, medium and large-sized particles were predominant, while D10 increased steadily with mass flow rate. The influence of density on particle size is depicted in Fig. 15 (d). Particle size varied dynamically with changes in density. The particle size parameters for steel slag with densities of 2800 kg/m^3 and 3200 kg/m^3 were similar, while those for densities of 3000 kg/m^3 and 3550 kg/m^3 were comparable, with D10 being 13.31 % higher than the former and D50 and D90 averaging 5.56 % higher. These findings indicated that by adjusting the gas quenching wind speed, viscosity, mass flow rate, and density, the particle size distribution of MSS can be effectively controlled to meet different application requirements, thus enhancing the reutilization and performance of steel slag products.

(2) Quantity of DPM particles under different conditions.

The quantity of particles produced by gas quenching was influenced by various factors, including operating conditions and the physical and chemical properties of the slag itself. Fig. 16 showed that with an increase in gas quenching wind speed, the number of steel slag particles initially increased and then decreased. The quantity of particles at wind speeds of 100 m/s and 200 m/s was comparable. Viscosity had a clear negative correlation with the number of particles produced by gas quenching. As viscosity increases, the number of particles decreases. When the viscosity was 1 Pa·s, the number of particles produced was 40.70 % less than when the viscosity was 0.25 Pa·s. In contrast, mass flow rate had the opposite effect on particle production. The increase in the total mass of liquid slag entering the granulation chamber resulted in more particles being produced, with a mass flow rate of 0.2 kg/s yielding 5,079 particles. The impact of density on the number of particles produced by gas quenching did not follow a clear pattern; the quantity fluctuated with changes in density. To visually analyze the granulation capacity of the gas quenching process under different influencing factors, we compared the total number of particles produced under various conditions. This comparison provided theoretical guidance for the metallurgical granulation industry and the high-value utilization of steel slag. Fig. 17 showed that using Case 3 as a reference, increasing the mass flow rate and controlling the slag density could effectively increase the number of particles produced. However, excessively high or low gas-quenching wind speeds and increased slag viscosity significantly reduce particle production. Among these four influencing factors, gas quenching wind speed, slag viscosity, and mass flow rate played dominant roles. Considering multiple factors in coordination is essential for optimizing and stabilizing the gas quenching granulation process.

(3) Total volume of DPM particles under different conditions.

The total volume of the steel slag particles can be considered as a function of both the individual particle size and the number of particles. The changes in both factors collectively determined the total volume. It can be said that the total volume of the steel slag particles directly reflected the granulation efficiency of the gas quenching process. As

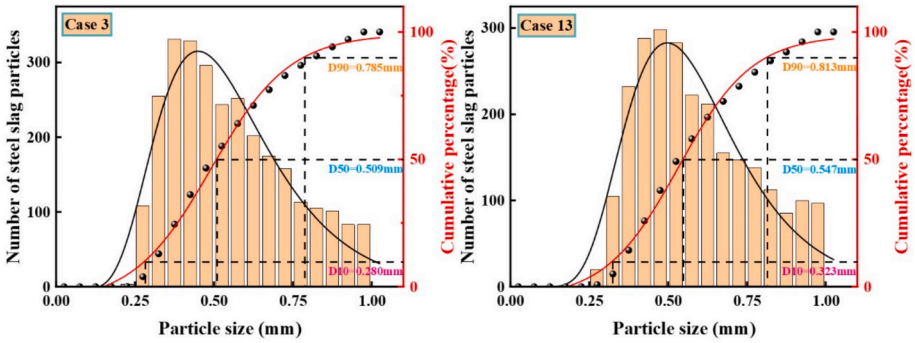

Fig. 14. Example of particle size distribution curves for cases 3 and 13 at 20 ms.

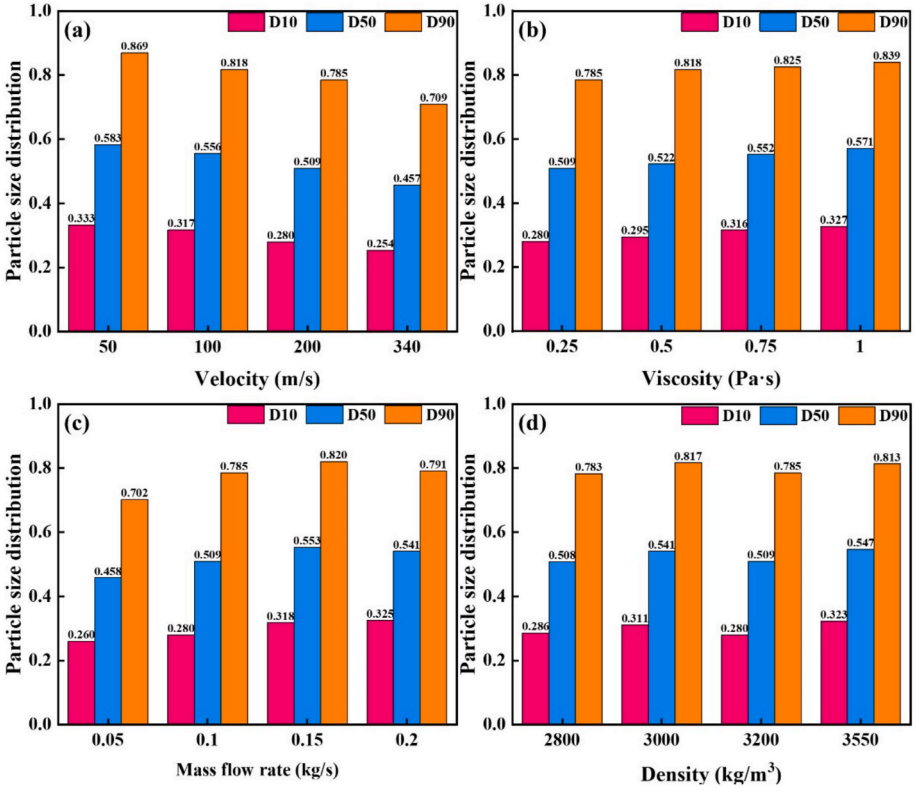

Fig. 15. Particle size of steel slag corresponding to D10, D50 and D90 at 20 ms for different working conditions at 20 ms.

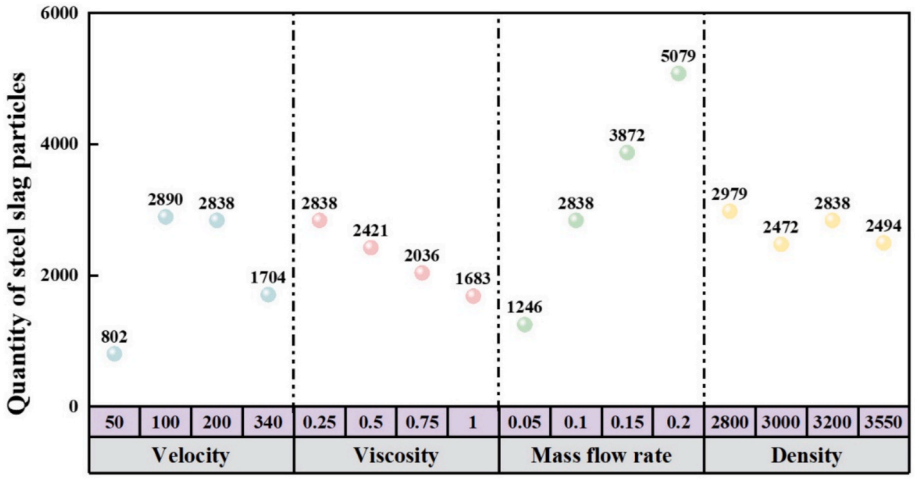

Fig. 16. Number of steel slag particles in the granulation chamber under different working conditions at 20 ms.

shown in Fig. 18, the total volume of the particles initially increased and then decreased with the increase in gas quenching velocity. The maximum total particle volume, 4.11×10^{-7} m^3, was observed at a gas-quenching velocity of 100 m/s. This was because, although the particle size decreased with increasing gas quenching velocity, the number of particles produced at 50 m/s was the smallest. As the viscosity increased, the particle size distribution generally expanded, but the total particle volume gradually decreased, which was also influenced by the number of particles. The mass flow rate had the most significant impact on the total particle volume, with the total volume at a mass flow rate of 0.20 kg/s being 5.61 times greater than that at 0.05 kg/s. The density of the MSS had a minimal effect on the total particle volume, with the overall fluctuation not exceeding 3.68 %. It is worth noting that when the MSS density was 3200 kg/m^3, the number of particles produced by gas quenching was 344 more than at a density of 3550 kg/m^3. However, the total volume of the particles was lower at the density of 3200 kg/m^3 than at 3550 kg/m^3. In this case, the particle size played a crucial role, with the size having a dominant influence on the total particle volume.

4.3. *Integrated information for the gas quenching process*

The gas quenching process of MSS was an extremely complex procedure, influenced by multiple factors. The fragmentation and granulation effects caused by different factors varied significantly. Identifying the key factors that affected the fragmentation and granulation process of MSS directly determined the granulation efficiency of steel slag and the quality of the final particles. Through a systematic analysis of the impact of various factors on all granulation characteristic parameters

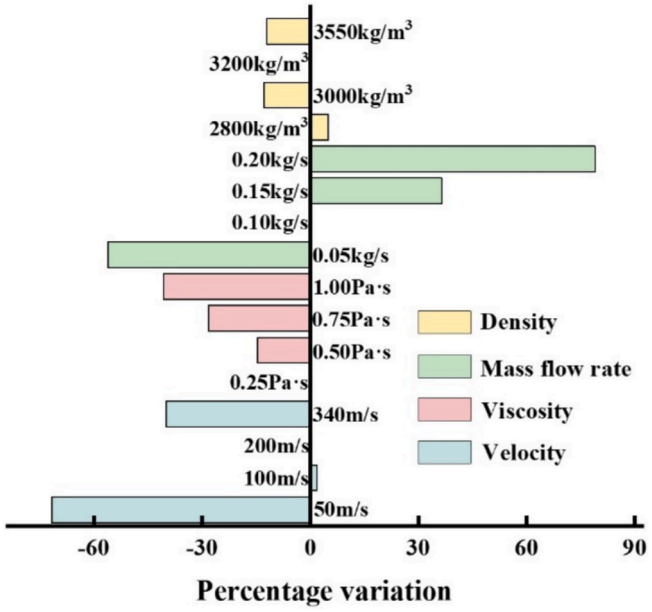

Fig. 17. Comprehensive comparison of pelletizing capacity under different working conditions.

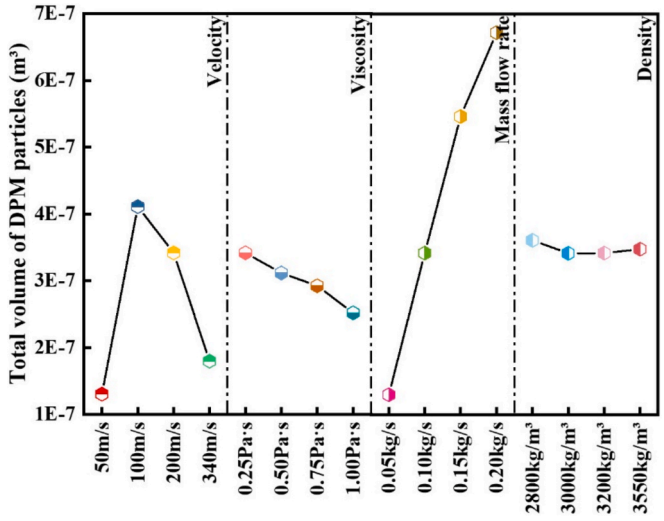

Fig. 18. Comparison of the total volume of steel slag particles under different working conditions at 20 ms.

during the gas quenching process, scientific data were provided to optimize process parameters and improve granulation efficiency. This study offered an important reference for further enhancing the resource utilization efficiency of steel slag and the precise control of the gas quenching process. We calculated the variance of MSS granulation characteristic parameters under different factors, using the size of the variance under different factor conditions as an indicator to assess the quality of the fragmentation and granulation effects. A larger variance indicated greater fluctuations or dispersion in the data, meaning that fluctuations in the factors were more likely to cause changes in the fragmentation and granulation effects, thus more directly influencing the results of the gas quenching process.

As shown in Fig. 19, the variances of the MSS granulation characteristic parameters under different factors were ranked. The six-pointed star represented the data with the largest variance, followed by the five-pointed star, four-pointed star, and triangle. It can be observed that the variance of the granulation characteristic parameters corresponding to gas quenching velocity was generally large, indicating that changes in gas quenching velocity were more likely to cause significant fluctuations in the granulation characteristic parameters. The mass flow rate of MSS had the second-largest influence on the granulation characteristic parameters, with a higher proportion of patterns representing high variance. The viscosity and density of MSS had relatively small effects on the granulation characteristic parameters, with a greater number of four-pointed star and triangle patterns. Additionally, a method for comprehensively considering the impact of different factors on the overall fragmentation effect of MSS was proposed. Values were assigned to each pattern, with the six-pointed star receiving 4 points, followed by 3 points, 2 points, and 1 point according to the represented variance size. The scores for all granulation characteristic parameters under different factors were calculated, and the results are shown in Fig. 20. As can be seen from the figure, gas quenching velocity was the primary factor influencing the MSS gas quenching process, followed by the mass flow rate of MSS. The viscosity and density of MSS had relatively minor impacts on the granulation process.

5. Conclusion

For the first time, the VOF to DPM model was successfully used to investigate the gas quenching process of MSS. The authenticity verification of simulation results has been verified with the help of on-site sampling measurements. Integrated information was summarized as follows:

(1) The use of high-resolution mesh successfully captures the fragmentation details of the gas quenching MSS process and allows for dynamic tracking of divergent particles in the DPM form.

(2) The morphological evolutions and the extent of the main steel jet's spread vary significantly corresponding to the main body region, non-mutual adhesion region and granulated particles region caused by the different combined effects of internal and external forces. Intrinsic connections are observed among different operating conditions, which highlight that the gas quenching velocity and the mass flow rate of MSS are the critical factors influencing the fragmentation performance.

(3) Considering multiple factors, the particle size distribution of steel slag can be effectively controlled to meet different application requirements. The particle size distribution and the validation of the simulation of the VOF to DPM model are well documented by actual industrial data.

With the continuous advancement of high-performance computing and multiphysics coupling technologies, the VOF to DPM based simulation of MSS gas granulation is expected to evolve in the following directions. First, expanding the model's adaptability to different slag compositions, nozzle geometries, and gas flow conditions through large-scale parametric studies combined with experimental calibration can promote the industrial application of simulation results across various steel plants. Second, by integrating population balance models (PBM) or machine learning approaches, a multiscale dynamic model that couples fragmentation and agglomeration mechanisms could be developed to enable real-time prediction of particle size distribution and online optimization of process parameters. In addition, reducing computational time while maintaining simulation accuracy to achieve real-time industrial simulations remains a key technical challenge to be addressed.

CRediT authorship contribution statement

Jiahao Zhang: Writing – original draft, Investigation, Formal analysis, Data curation, Conceptualization. **Jingcai Chang:** Writing – review & editing, Resources, Project administration, Formal analysis. **Yuke Li:** Validation, Methodology, Investigation. **Zongqiang Li:** Supervision, Software, Investigation. **Taiyang Liu:** Methodology, Investigation, Funding acquisition. **Fenghua Wei:** Investigation, Funding acquisition. **Peng Wang:** Visualization, Validation, Formal analysis. **Hongfei wu:** Funding acquisition.

		Velocity	Viscosity	Mass flow rate	Density
Continuous phase	Length				
	Width				
	Average liquid film thickness				
	Number of discrete liquid blocks				
	Maximum size of discrete liquid block				
Discrete phase	Average particle size				
	Number of particles				
	Total particle volume				
Note	Order of variance from largest to smallest				

Fig. 19. Schematic of the ranking of the variance in the MSS granulation characteristic parameters under different conditions.

Fig. 20. Extent of influence of different factors on the MSS gas quenching process.

Declaration of competing interest

The authors declare that they have no known competing financial interests or personal relationships that could have appeared to influence the work reported in this paper.

Acknowledgment

This work was supported by the National Natural Science Foundation of China (22478227), Shandong Provincial Natural Science Foundation (ZR2021ME049), and Taishan Industry Leading Talents Project (Tscx202306135).

Data availability

Data will be made available on request.

References

Li, Y., Liu, F., Yu, F., Du, T., 2024. A review of the application of steel slag in concrete. Structures 63, 106352. https://doi.org/10.1016/j.istruc.2024.106352.

Gao, Y., Hao, J., Peng, J., et al., 2023. Treatment process and comprehensive utilization of steel slag. China Foundry Equipment & Technology 58, 39–45. https://doi.org/10.3969/j.issn.1006-9658.2023.05.008.

Li, W., Cao, M., Wang, D., Chang, J., 2023. Increase in volume stability of RO phases in steel slag by combined treatment of alkali and dry carbonation. Constr. Build. Mater. 396, 132345. https://doi.org/10.1016/j.conbuildmat.2023.132345.

Lv, M., Chen, S., Yang, L., Wei, G., 2022. Research progress on injection technology in converter steelmaking process. Metals 12, 1918. https://doi.org/10.3390/met12111918.

Wang, G., Wang, Y., Gao, Z., 2010. Use of steel slag as a granular material: volume expansion prediction and usability criteria. J. Hazard. Mater. 184, 555–560. https://doi.org/10.1016/j.jhazmat.2010.08.071.

Srivastava, S., Cerutti, M., Nguyen, H., Carvelli, V., Kinnunen, P., Illikainen, M., 2023. Carbonated steel slags as supplementary cementitious materials: reaction kinetics and phase evolution. Cem. Concr. Compos. 142, 105213. https://doi.org/10.1016/j.cemconcomp.2023.105213.

Wu, L., Liu, K., Rao, L., Wang, J., Wang, H., 2021. Effect of binary basicity and ferric oxide content on the soundness, grindability, and cementitious activity of converter steelmaking slag. Constr. Build. Mater. 300, 124287. https://doi.org/10.1016/j.conbuildmat.2021.124287.

Yao, X., Liu, Y., Yu, Q., Wang, S., 2023. Energy consumption of two-stage system of biomass pyrolysis and bio-oil reforming to recover waste heat from granulated BF slag. Energy 273, 127204. https://doi.org/10.1016/j.energy.2023.127204.

Gu, W., Diao, J., Jiang, L., Yu, H., Tan, W., Chen, L., Li, H., Xie, B., Ueda, S., 2024. Phase development in steelmaking slags during a gas quenching granulation process. J. Environ. Chem. Eng. 12, 112504. https://doi.org/10.1016/j.jece.2024.112504.

Dayioglu, A.Y., 2024. pH-dependent leaching characteristics of steel slag mitigated with water treatment residual. Geotech. Test. J. 47. https://doi.org/10.1520/GTJ20220288.

Zhang, D., Ma, T., 2022. Study on slagging in a waste-heat recovery boiler associated with a bottom-blown metal smelting furnace. Energy 241, 122852. https://doi.org/10.1016/j.energy.2021.122852.

R. Safavi Nick, V. Leinonen, J. Mäyrä, J. Björkvall, Towards Greener Industry: Modelling of Slag Heat Recovery, Metals 11 (2021) 1144. doi: 10.3390/met11071144.

Yang, P., Ma, C., Ma, G., Zhang, B., Zhang, R., Yang, B., Wu, Z., 2024. Waste heat recovery of blast furnace slag in moving bed: influencing of structural parameters and operating parameters. Int. J. Heat Fluid Flow 107, 109421. https://doi.org/10.1016/j.ijheatfluidflow.2024.109421.

Zhang, T., 2023. Modeling, validation and industrial testing of heat transfer for waste heat recovery from hot converter steel slag. University of Science and Technology Beijing.

Liu, G., Tang, Y., Wang, J., 2022. Effects of carbonation degree of semi-dry carbonated converter steel slag on the performance of blended cement mortar – reactivity, hydration, and strength. J. Build, Eng.

Sakhvadze, D., Jandieri, G., Jangveladze, G., Sakhvadze, G., 2021. A new technological approach to the granulation of slag melts of ferrous metallurgy: obtaining glassy fine-grained granules of improved quality. J. Eng Appl. Sci. (online) 68, 1–17. https://doi.org/10.1186/s44147-021-00019-7.

Özbay, E., Erdemir, M., Durmuş, H.0., 2016. Utilization and efficiency of ground granulated blast furnace slag on concrete properties - a review. Constr. Build. Mater. 105, 423–434. https://doi.org/10.1016/j.conbuildmat.2015.12.153.

K.G. Judd, K. Tsaknopoulos, B.C. Sousa, M. Pepi, D.L. Cote, Comparative Evaluation of Titanium Feedstock Powder Derived from Recycled Battlefield Scrap vs. Virgin Powder for Cold Spray Processing, Materials 17 (2024). doi: 10.3390/ma17051122.

Wu, J., Xia, M., Wang, J., Zhao, B., Ge, C., 2023. Effect of electrode induction melting gas atomization on powder quality: satellite formation mechanism and pressure. Materials 16. https://doi.org/10.3390/ma16062499.

Anderson, I.E., White, E.M.H., Dehoff, R., 2018. Feedstock powder processing research needs for additive manufacturing development. Curr. Opin. Solid State Mater. Sci. 22, 8–15. https://doi.org/10.1016/j.cossms.2018.01.002.

Foti, D., Giorno, S., Duraisamy, K., 2020. An adaptive mesh refinement approach based on optimal sparse sensing. Theor. Comput. Fluid Dyn. 34, 457–482. https://doi.org/10.1007/s00162-020-00522-2.

Wang, L., 2021. Research on granulation mechanism and heat transfer characteristics of gas quenching blast furnace slag. University of Science and Technology, North China.

Long, Y., Cai, Z., Zhang, Y., et al., 2013. Numerical simulation of liquid steel slag gas quenching granulation process. Shanghai Metals 35, 38–42. https://doi.org/10.3969/j.issn.1001-7208.2013.06.010.

Ming, J., 2021. Research on the heat exchange law of steel slag air quenching process and process line improvement. University of Science and Technology, North China.

Wang, L., Zhang, Y., Long, Y., et al., 2020. Numerical simulation of liquid film flow characteristics of gas-quenched granulated blast furnace slag, Journal of. Process. Eng. 20, 887–895.

Liu, X., Wen, Z., Dun, Y., et al., 2022. Study on liquid film crushing process of gas quenching and granulation slag. Journal of Central South University (natural Science Edition) 53, 2851–2860. https://doi.org/10.11817/j.issn.1672-7207.2022.08.004.

Liu, Q., Wang, X., Zhang, J., Xu, Y., Yang, Q., Xiong, Q., Han, L., Zhou, Y., 2025. CFD-VOF-DPM modeling and spatiotemporal analysis of particle sedimentation behaviors in gas-liquid-solid fluidized bed reactor. Chem. Eng. Sci. 305, 121161. https://doi.org/10.1016/j.ces.2024.121161.

Liu, J., Ke, P., 2022. Modelling and analysis of initial icing roughness with fixed-grid enthalpy method based on DPM-VOF algorithm. Chin. J. Aeronaut. 35, 168–178. https://doi.org/10.1016/j.cja.2021.07.028.

Harizi, W., Hamdi, F., Chrigui, M., 2024. A comprehensive numerical investigation of the spray characteristics in spill-return atomizers using coupled VOF and Euler-Lagrange approach. Particuology 95, 319–332. https://doi.org/10.1016/j.partic.2024.10.010.

Sun, J., Zhang, J., Jiang, R., Feng, X., Liu, Q., 2024. Numerical simulation of droplet splashing behavior in steelmaking converter based on VOF-to-DPM hybrid model and AMR technique, metallurgical and materials transactions. B, Process Metallurgy and Materials Processing Science 55, 1098–1116. https://doi.org/10.1007/s11663-024-03024-2.

Liu, A., Wen, H., Yu, H., 2023. Characterization of Fuel Flow and Atomization in Centrifugal Nozzles Based on VOF-DPM Models. Thermal Power Engineering 38, 106–114. https://doi.org/10.16146/j.cnki.rndlgc.2023.11.013.

Morsi, S.A., Alexander, A.J., 1972. An investigation of particle trajectories in two-phase flow systems. J. Fluid Mech. 55, 193. https://doi.org/10.1017/S0022112072001806.

Li, L., Wei, G., Zhu, Z., Li, B., 2023. Simulation of slag droplet entrainment by volume of fluid and lagrangian particle tracking coupled modeling. ACS Omega 8, 28290–28300. https://doi.org/10.1021/acsomega.3c02159.

Di Martino, M., Ahirwal, D., Maffettone, P.L., 2022. Computational fluid dynamics characterization of the hollow-cone atomization: newtonian and non-newtonian spray comparison. Physics of Fluids Physics of Fluids 34. https://doi.org/10.1063/5.0104658.

Yan, S., Zhang, X., Luo, Z., 2025. Adaptive mesh refinement for VOF modeling gas-liquid two-phase flow: a summary of some algorithms and applications. Chem. Eng. Sci. 306, 121291. https://doi.org/10.1016/j.ces.2025.121291.

Pappa, A., Verhaeghe, A., Bénard, P., De Paepe, W., Bricteux, L., 2024. Adaptive mesh refinement towards optimized mesh generation for large eddy simulation of turbulent combustion in a typical micro gas turbine combustor. Energy 301, 131550. https://doi.org/10.1016/j.energy.2024.131550.

Chen, D., Kumar, P., Kametani, Y., Hasegawa, Y., 2024. Multi-objective topology optimization of heat transfer surface using level-set method and adaptive mesh refinement in OpenFOAM. Int. J. Heat Mass Transf. 221, 125099. https://doi.org/10.1016/j.ijheatmasstransfer.2023.125099.

C. Xu, X. Zhou, H. Ren, S. Sutulo, C. Guedes Soares, Real-time calculation of ship to ship hydrodynamic interaction in shallow waters with adaptive mesh refinement, Ocean Eng. 295 (2024) 116943. doi: 10.1016/j.oceaneng.2024.116943.

Irigaray, O., Ansa, Z., Fernandez-Gamiz, U., Larrinaga, A., García-Fernandez, R., Portal-Porras, K., 2024. Adaptive mesh refinement (AMR) criteria comparison for the DrivAer model. Heliyon 10, e31966. https://doi.org/10.1016/j.heliyon.2024.e31966.

Chen, W., Ren, Y., Zhang, L., Scheller, P.R., 2019. Numerical simulation of steel and argon gas two-phase flow in continuous casting using LES + VOF + DPM model. JOM 71, 1158–1168. https://doi.org/10.1007/s11837-018-3255-8.

Heinrich, M., Schwarze, R., 2020. 3D-coupling of volume-of-fluid and lagrangian particle tracking for spray atomization simulation in OpenFOAM. SoftwareX 11, 100483. https://doi.org/10.1016/j.softx.2020.100483.

Radford, D.W., 1995. Volume fraction gradient induced warpage in curved composite plates. Compos. Eng. 5, 923–934. https://doi.org/10.1016/0961-9526(95)00033-J.

Chen, X., Zhang, X., 2016. An improved 3D MoF method based on analytical partial derivatives. J. Comput. Phys. 326, 156–170. https://doi.org/10.1016/j.jcp.2016.08.051.

Mohan, A., Tomar, G., 2021. Interface reconstruction and advection schemes for volume of fluid method in axisymmetric coordinates. J. Comput. Phys. 446, 110663. https://doi.org/10.1016/j.jcp.2021.110663.

W. Gu, Research on the flight dynamics and solidification heat transfer law of liquid steel slag air quenching process, Chongqing University, 2021. https://d.wanfangdata.com.cn/thesis/ChJUaGVzaXNOZXdTMjAyNDAxMDkSCUQwMjQzMDE1ORoIanh2bGsxYzI%3D.

Gao, C., Hao, S., Jiang, W., et al., 2015. Thermodynamic study of zinc-containing dust from molten steel slag sensible heat treatment. Metallurgical Energy 14–18.

Garoosi, F., Hooman, K., 2022. Numerical simulation of multiphase flows using an enhanced Volume-of-Fluid (VOF) method. Int. J. Mech. Sci. 215, 106956. https://doi.org/10.1016/j.ijmecsci.2021.106956.

Hirt, C.W., Nichols, B.D., 1981. Volume of fluid (VOF) method for the dynamics of free boundaries. J. Comput. Phys. 39, 201–225. https://doi.org/10.1016/0021-9991(81)90145-5.